ACS Catalysis
Research Article
Cite This: *ACS Catal.* 2018, 8, 8578−8589
pubs.acs.org/acscatalysis

Selectivity Modulation of Encapsulated Palladium Nanoparticles by Zeolite Microenvironment for Biomass Catalytic Upgrading

Yuchao Chai,[†,‡] Sihang Liu,[§] Zhi-Jian Zhao,[§] Jinlong Gong,[§] Weili Dai,[†,‡] Guangjun Wu,[†,‡] Naijia Guan,[†,‡] and Landong Li*[,†,‡]

[†]School of Materials Science and Engineering, National Institute for Advanced Materials, Nankai University, Tianjin 300350, China

[‡]Key Laboratory of Advanced Energy Materials Chemistry of Ministry of Education, Collaborative Innovation Center of Chemical Science and Engineering, Nankai University, Tianjin 300071, China

[§]Key Laboratory for Green Chemical Technology of Ministry of Education, School of Chemical Engineering and Technology, Tianjin University, Tianjin 300072, China

Supporting Information

ABSTRACT: Metal nanoparticles encapsulated in zeolite have been recently developed as a special type of catalyst that shows significant advantages in activity, shape-selectivity, and stability over conventional supported catalysts. The selectivity modulation of encapsulated nanoparticle catalysis by the zeolite microenvironment is theoretically possible but not addressed yet. Here, we report the in situ encapsulation of sub-nanometric palladium species within MFI-type zeolites, which exhibit high activity and good stability in the hydroconversion of furfural as a model reaction of biomass upgrading. Remarkably, different products, e.g., furan, furfural alcohol, and 1,5-pentanediol, from furfural hydroconversion can be obtained when silicalite-1, Na-ZSM-5, and H-ZSM-5 are employed as hosts of palladium nanoparticles, respectively. Density functional theory calculations and spectroscopy investigations reveal that both the adsorption of furfural and the activation of hydrogen are significantly affected by the zeolite microenvironment, leading to different reaction pathways. Our work presents an elegant example of catalytic selectivity modulation of encapsulated metal nanoparticles by tuning the zeolite microenvironment.

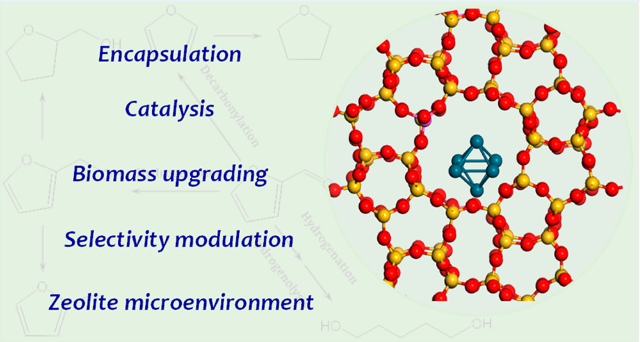

KEYWORDS: *encapsulation, palladium nanoparticles, zeolite microenvironment, furfural hydroconversion, selectivity modulation*

1. INTRODUCTION

Supported metal catalysts, a most common type of materials employed in heterogeneous catalysis, play a critical role in the sustainable production of fuels and chemicals. The performance of supported metal catalysts is controlled by many interrelated factors, e.g., the intrinsic properties of metal centers, the sizes of metal particles, the functionalities of supports, and the interaction between metals and supports, which make supported metal catalysts very complicated systems to interpret.[1−3] In addition, the reconstruction and sintering of metal particles during reaction contributes to an important issue of supported metal catalysts.[4−6]

Zeolites are widely used support materials for metal centers that can provide fine-tuned acid−base sites, special electronic interactions, and well-defined channels for catalytic processes.[7] Metal nanoparticles encapsulated in zeolites have been recently developed as a unique type of supported metal catalyst.[8−19] The steric restrictions from zeolite channels can effectively suppress the aggregation of metal particles during both catalyst preparation and catalytic reaction processes, generating highly active zeolite-encapsulated uniform metal particles with remarkable stability against sintering.[8−16] Moreover, compared with metal particles on the outer surface of zeolites, zeolite-encapsulated metal nanoparticles exhibit attractive substrate-shape selectivity in catalytic reactions.[17−20] It seems that zeolite-encapsulated nanoparticles can hopefully address most of the important issues of supported catalysts, i.e., activity, selectivity, and stability. But this is far from the end of the story. Zeolites are not inert supports, and they can provide a specific microenvironment, e.g., confinement effects and functional sites, for catalytic reactions. The confinement effects can modulate the properties of metal nanoparticles, which accordingly result in different catalytic properties. The functional sites, e.g., acid−base sites, are in close proximity with the encapsulated nanoparticles and can further alter their properties. However, to our knowledge, the impacts of the zeolite microenvironment on the catalytic behaviors of

Received: June 11, 2018
Revised: July 21, 2018
Published: August 6, 2018

DOI: 10.1021/acscatal.8b02276
ACS Catal. 2018, 8, 8578−8589

encapsulated metal nanoparticles are not well understood so far.

Here, we report the in situ encapsulation of palladium nanoparticles in MFI-type zeolites and the construction of robust catalysts on the basis of encapsulated palladium nanoparticles and MFI zeolite microenvironment. The catalyst systems are applied in the hydroconversion of furfural (FFL), which is an important biomass-derived platform molecule that can be transformed into several value-added chemicals, e.g., furfural alcohol (FAL), 2-methylfuran (2-MF), and furan.[21−23] Significantly, we demonstrate, for the first time, the selectivity modulation of palladium catalysis by a zeolite microenvironment, which can shed a light on the rational design of zeolite-encapsulated noble metal nanoparticles for selective catalysis.

2. EXPERIMENTAL SECTION

2.1. Chemical Reagents. The following reagents were directly used without further purification: silica solution (50 wt % SiO_2, Alfa Aesar), sodium aluminate ($NaAlO_2$, J&K), tetrapropylammonium hydroxide solution (TPAOH, 40 wt % in water, Macklin), sodium hydroxide (NaOH, J&K), $Pd(NO_3)_2$ solution (40.1 wt % in methanol, Aladdin), (3-mercaptopropyl)trimethoxysilane (MPTS, Adamas), ammonium nitrate (NH_4NO_3, J&K), sodium nitrate ($NaNO_3$, J&K), nitrobenzene (99%, J&K), 1-nitronaphthalene (98%, J&K), sodium borohydride (98%, J&K), 4-methoxyphenylboronic acid (98%, J&K), iodobenzene (98%, TCI), 2,4,6-trimethyl iodobenzene (97%, J&K), potassium carbonate (99%, J&K), 2-propanol (99%, Alfa Aesar), furfural (99%, Alfa Aesar), and *n*-dodecane (99%, Acros).

2.2. Encapsulation of Palladium Nanoparticles in MFI Zeolites. *Pd-SH Precursor.* Pd-SH precursor was prepared from $Pd(NO_3)_2$ and MPTS in a mixed solution of ethanol and H_2O (v/v = 1:1, called mixed-solvent strategy). In a typical experiment, 2.5 g of MPTS was dissolved in the mixture solution of 10 mL of H_2O and 10 mL of ethanol. Then 1.82 g of $PdNO_3$ (40.1 wt %) was added dropwise into the previous solution under stirring.

Raw Pd@ZSM-5. Raw Pd@ZSM-5 was synthesized via a simple hydrothermal process. In a typical experiment, 1.02 g of NaOH and 0.45 g of $NaAlO_2$ were added into 100 mL of deionized water with 0.8 g of TPAOH solution and stirred for 15 min at room temperature. SiO_2 gel (10 g, 50 wt %) was then added into above solution. After being stirred for 30 min, 3 mL of Pd-SH precursor solution was added dropwise into the above mixture, which was fully hydrolyzed at 80 °C for 6 h under stirring to form synthesis gel (called prehydrolysis strategy). Finally, the gel with a molar ratio of 1 SiO_2/0.02 Al_2O_3/0.15 Na_2O/0.04 TPAOH/0.005 Pd-SH/100 H_2O was transferred into an autoclave and heated at 170 °C for 3 days under static conditions. The solid sample was collected by centrifuging, washing with water, and drying at 80 °C overnight to derive raw Pd@ZSM-5.

Pd@Na-ZSM-5 and Pd@H-ZSM-5. Raw Pd@ZSM-5 was ion exchanged with 1 M $NaNO_3$ or NH_4NO_3 solution three times, dried at 80 °C overnight, calcined in flowing air at 550 °C for 6 h (Figure S1), and finally reduced in 10%H_2/Ar at 240 °C for 2 h to derive the Pd@Na-ZSM-5 or Pd@H-ZSM-5 sample, respectively.

Pd@S-1. Pd@S-1 was synthesized from similar to those employed in the synthesis of Pd@H-ZSM-5, except that no aluminum precursor was added throughout the process.

Pd/S-1, Pd/Na-ZSM-5, and Pd/H-ZSM-5. Palladium species were also introduced into S-1, Na-ZSM-5, and H-ZSM-5 zeolites by wet impregnation, followed by similar drying, calcination, and reduction steps. The final products were denoted as Pd/S-1, Pd/Na-ZSM-5, and Pd/H-ZSM-5, respectively.

2.3. Characterization Techniques. The X-ray diffraction (XRD) patterns of zeolite samples were recorded on a Bruker D8 diffractometer using Cu Kα radiation ($\lambda = 0.1541$ nm) at a scanning rate of 6°/min in the region of $2\theta = 5-50°$.

The surface areas of zeolite samples were determined by nitrogen adsorption/desorption isotherms at −196 °C collected on a Quantachrome iQ-MP gas adsorption analyzer. The total surface area was calculated via the Brunauer−Emmett−Teller (BET) equation, and micropore size distribution was determined using the t-plot method.

Solid-state nuclear magnetic resonance (NMR) experiments were performed on a Bruker Advance III 400WB spectrometer at resonance frequencies of 104.3 and 79.5 MHz for ^{27}Al and ^{29}Si NMR, respectively.

Samples for electron microscopy analysis were prepared by drying a drop of sample-containing alcohol suspension on carbon-coated copper grids. High angle annular dark field scanning transmission electron microscopy (HAADF-STEM) images were acquired on a FEI Talos electron microscope. The relatively large collection angle (54−200 mard) of the HAADF-STEM detector ensures the excellent atomic-number (Z) sensitivity.[24] Since zeolite crystals are quite sensitive to electron beams, under HAADF mode, we reduced the probe size to 10 (beam current: ~16 pA) for high-quality HAADF imaging. Mapping the elemental distribution of zeolite crystals was conducted under HAADF-STEM mode using FEI built-in energy dispersive spectrum (EDS) software with drift correction applied. The average palladium nanoparticle diameters in the images were calculated by surface-area-weighted, $d_{TEM} = \sum n_i d_i^3 / \sum n_i d_i^2$.

The experiments of temperature-programmed reduction by hydrogen (H_2-TPR) were performed on a Quantachrome ChemBET 3000 chemisorption analyzer. In a typical experiment, the sample was calcined in dry air at 550 °C for 1 h and cooled to 50 °C in flowing Ar. The H_2-TPR profile was recorded in flowing 5%H_2/Ar at a heating rate of 10 °C/min from 50 to 400 °C.

X-ray photoelectron spectra (XPS) of palladium containing samples were recorded on a Thermo Scientific ESCALAB 250Xi spectrometer using monochromatic Al Kα X-ray source ($h\nu = 1486.6$ eV) as the excitation source. Accurate binding energies (±0.1 eV) were determined with respect to the position of the adventitious C 1s peak at 284.8 eV.

FTIR spectra of CO adsorption on samples were recorded on a Bruker Tensor 27 spectrometer. In a typical experiment, a self-supporting sample pellet was placed in the reaction chamber, and the background spectrum was taken at 25 °C in flowing He. Afterward, the sample was saturated with 1% CO/He and purged with He at the same temperature for 1 h. The steady-state FTIR spectrum of CO adsorption on sample was finally recorded with the resolution of 4 cm^{-1}.

The experiments of temperature-programmed desorption of ammonia (NH_3-TPD) were performed on a Quantachrome ChemBet 3000 chemisorption analyzer. In a typical experiment, the sample was saturated with 5% NH_3/He at 50 °C and then purged with He at the same temperature for 1 h to eliminate the physical absorbed ammonia. The NH_3-TPD

DOI: 10.1021/acscatal.8b02276
ACS Catal. 2018, 8, 8578−8589

profile was recorded in flowing He at a heating rate of 10 °C/min from 50 to 800 °C.

The experiments of temperature-programmed desorption of carbon dioxide (CO_2-TPD) were also performed on the Quantachrome ChemBet 3000 chemisorption analyzer. In a typical experiment, the sample was saturated with 5% CO_2/He at 50 °C and then purged with He at the same temperature for 1 h to eliminate the physical absorbed carbon dioxide. CO_2-TPD profile was recorded in flowing He at a heating rate of 10 °C/min from 50 to 800 °C.

The experiments of temperature-programmed desorption of hydrogen (H_2-TPD) were also performed on the Quantachrome ChemBet 3000 chemisorption analyzer. In a typical experiment, the sample was saturated with 10% H_2/Ar at 50 °C and then purged with Ar at the same temperature for 1 h to eliminate the physical absorbed hydrogen. H_2-TPD profile was recorded in flowing Ar at a heating rate of 10 °C/min from 50 to 700 °C

The experiments of temperature-programmed desorption of furfural (FFL-TPD) were also performed in the fixed-bed reactor connected with a downstream gas sampling mass spectrometer (Pfeiffer Omnistar). In a typical experiment, the sample was saturated with furfural at 60 °C in a He flow (20 mL/min) and then purged with He at the same temperature for 1 h to eliminate the physical absorbed furfural. The FFL-TPD profile was recorded in flowing He at a heating rate of 10 °C/min from 60 to 700 °C.

2.4. Catalytic Studies. The hydroconversion of FFL was performed in a high-pressure stainless autoclave (Xinyuan Chemical Machinery, Series CJK, 300 mL) at a stirring rate of 750 rpm, which is adequate to exclude the external mass transfer limitation. In a typical experiment, 1.2 g of catalyst, 24 mmol of FFL, and 90 mL of 2-propanol were well mixed in the autoclave and purged with pure He three times at room temperature. The autoclave was rapidly heated to the designated temperature, and then hydrogen was introduced at 1 MPa to initiate the reaction.

After reaction, the liquid organic products were analyzed by gas chromatography (Shimadzu GC-2010) and gas chromatography−mass spectrometry (Shimadzu GCMS-QP2010 SE), both with a RXI-5MS column (30 m, 0.25 mm i.d., stationary phase thickness of 0.25 μm). *n*-Dodecane was used as an internal standard for quantification. The possible gas products were analyzed with a mass spectrometer (Pfeiffer Omnistar GSD 320).

Recycling tests in FFL hydroconversion over Pd@Na-ZSM-5 catalyst were conducted. In a typical experiment, the mixture after one reaction cycle (6 h) was centrifuged at 8000 rpm to deposit the solid catalyst, which was washed with CH_2Cl_2 and dried at 80 °C for 12 h for next use directly.

The conversion, selectivity, and reaction rate are defined as follows:

$$\text{FFL conversion (\%)} = \frac{\text{FFL}_{\text{before}} - \text{FFL}_{\text{after}}}{\text{FFL}_{\text{before}}} \times 100$$

$$\text{product selectivity (\%)} = \frac{\text{product}_{\text{after}}}{\text{FFL}_{\text{before}} - \text{FFL}_{\text{after}}} \times 100$$

$$\text{reaction rate (mmol/g/h)} = \frac{\text{FFL}_{\text{before}} - \text{FFL}_{\text{after}}}{m_{\text{catalyst}} \times \text{time}}$$

2.5. Theoretical Calculations. Density functional theory (DFT) calculations were performed with the plane wave-based Vienna ab initio simulation package, VASP.[25] The calculations took advantage of the generalized gradient approximation (GGA) in the form of the Bayesian error estimation functional with van der Waals correlation (BEEF-vdW).[26] The projector augmented wave (PAW) method was applied to depict the interaction between the atomic electrons and cores.[27]

The well-tested genetic algorithms were applied in our global optimization method.[28,29] A unit-cell of $Si_{94}Al_2O_{192}$ was used to represent the MFI framework with the aluminum atoms located in calculated stable positions. To boost the convergence procedure, the global optimization calculations were conducted with a reduced energy cutoff of 300 eV, and Brillouin zone-sampling was restricted to the Γ point. The geometries in global optimization calculations were relaxed until the force on every atom was less than 0.05 eV/Å. The obtained possible global minima were later refined with a cutoff of 400 eV and a force convergence standard of 0.02 eV/Å. The initial candidates of Pd clusters in generation 0 were randomly generated by the algorithms with the constraint for minimal atom distances and unit-cell spacing. Each generation produced 10 well-optimized structures, which were then added into the competing list for the "fitness test". The 10 structures of the former generations with lowest energies (10 "fittest" candidates) would be selected for mating and then reproduced the next generation. To produce as many different configurations as possible, the mutation was introduced to trigger a 20% possibility for each structure to swag atom positions. And an exponential fitness function with $\alpha = 3$ was applied to pass down the structural information from parent generation according to roulette wheel selection method.[29]

According to results from global optimization and spectroscopy characterizations, stable Pd_4 and Pd_6 were employed to simulate palladium nanoparticles encapsulated in S-1, and Na-ZSM-5. A 201-atom cubooctahedral cluster (Pd_{201}) was used to simulate Pd nanoparticles supported on S-1. The adsorption energy is defined as $E_{\text{FFL}} = E(\text{X} + \text{FFL}) - E(\text{X}) - E(\text{FFL})$. $E(\text{FFL})$ is the energy of a gas-phase FFL molecule, and $E(\text{X})$ is the energy of bare X, where X represents Pd/S-1, Pd@S-1, or Pd@Na-ZSM-5.

3. RESULTS AND DISCUSSION

3.1. Synthesis and Characterization of Zeolite-Encapsulated Palladium Nanoparticles. The in situ encapsulation of ligand-stabilized metal precursor during the hydrothermal synthesis of zeolite has been well documented, and zeolite-encapsulated nanoparticles can be obtained through a subsequent calcination and reduction process. However, a lack of productivity and reproducibility is always claimed. This becomes more prominent in the encapsulation of ligand-stabilized metal precursors in high-silica zeolites, e.g., ZSM-5, where higher alkalinity and crystallization temperature are employed. In this work, we improved the conventional synthesis route to zeolite-encapsulated palladium nanoparticles with two modifications, i.e., the mixed-solvent strategy during the preparation of ligand-stabilized palladium precursor and the prehydrolysis strategy in the crystallization step (see the Experimental Section for details). Briefly, Pd-SH precursor dissolved well in alcohol−water mixed solvent to form a clear solution even at a high temperature of 80 °C, and homogeneous gel was formed through the prehydrolysis process. As a result, zeolite-encapsulated palladium nano-

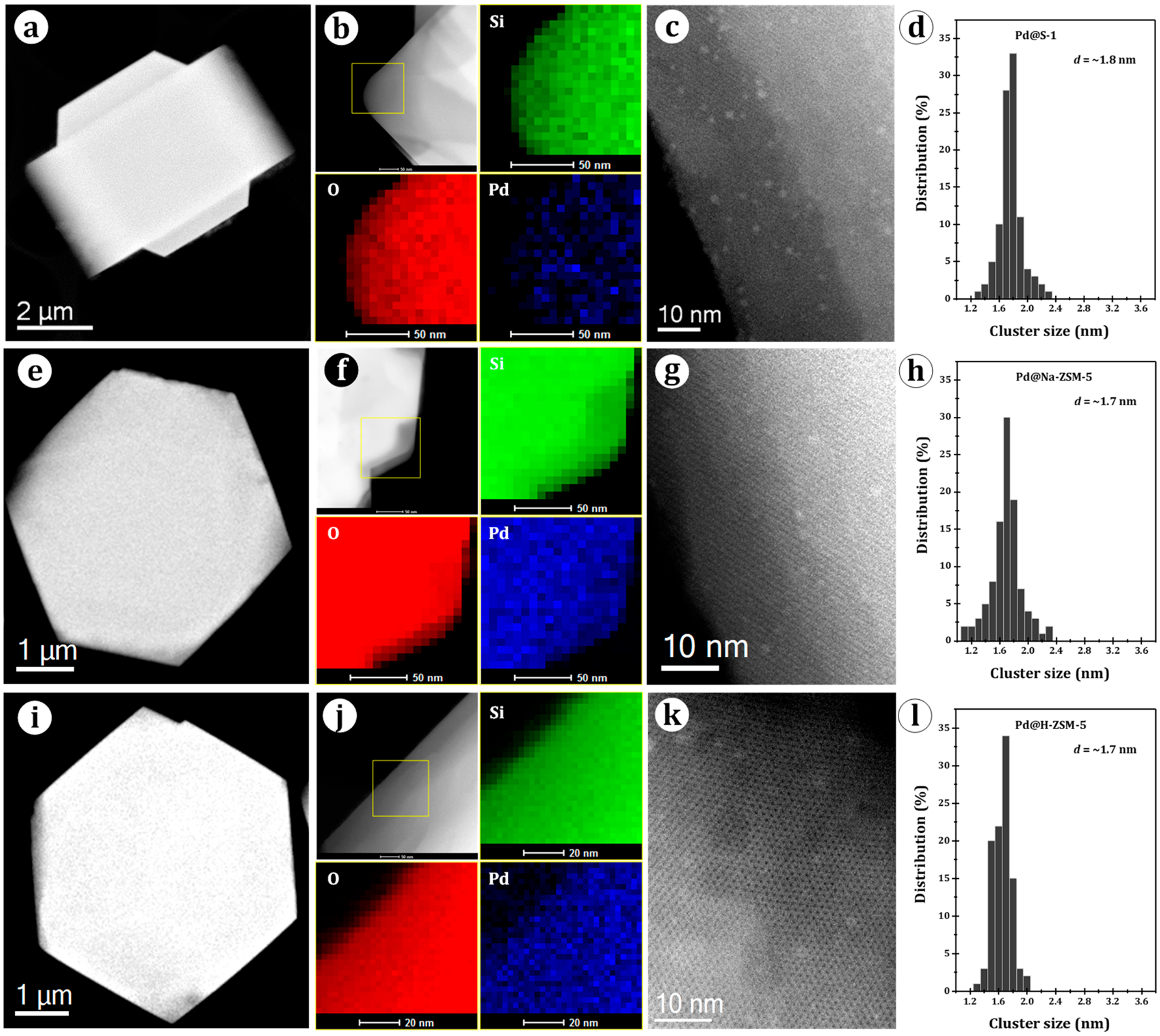

Figure 1. HAADF-STEM images, selected-area element mapping analyses, and high-resolution HAADF-STEM images of Pd@S-1 (a−c), Pd@Na-ZSM-5 (e−g), and Pd@H-ZSM-5 (i−k) with corresponding size distribution histograms of palladium nanoparticles (d, h, l).

particles with productivity of >90% and perfect reproducibility could be obtained. The actual palladium loadings in as-obtained zeolite encapsulated palladium nanoparticles, from both XRF and TEM-EDS analysis, matched well with the target palladium loadings (Table S1). XRD patterns of zeolite-encapsulated palladium nanoparticles (Figure S2) confirmed the pure phase of MFI type zeolites obtained and the nitrogen sorption isotherms revealed the high surface areas and large micropore volumes of the products (Figure S3 and Table S1). According to the nitrogen sorption isotherms, some mesopores were also created within zeolite crystals probably during the calcination removal of MPTS. Moreover, ^{29}Si/^{27}Al MAS NMR spectra (Figure S4) excluded the presence of nonframework silicon or aluminum species in the products.

The formation of encapsulated palladium nanoparticles in zeolite crystals were directly observed by electron microscopy (Figure 1). Low-magnification HAADF-STEM images (Figure 1a,e,i) revealed the well-shaped microscale zeolite single crystals of Pd@S-1, Pd@Na-ZSM-5, and Pd@H-ZSM-5, respectively, while no traces of palladium particles could be identified. Selected-area element mapping analyses undoubtedly confirmed the existence and the homogeneous dispersion of palladium species in the as-obtained zeolite samples. In the thin region (Figure 1b), well isolated palladium species could be directly observed, while homogeneous dispersion of palladium species without significant aggregation could be observed in the thick region (Figure 1f,j. In the high-resolution HAADF-STEM images, uniform palladium nanoparticles with mean size of 1.7−1.8 nm, i.e., the bright dots in the images, were well dispersed in zeolite crystals (Figure 1a,e,i). That is, uniform palladium nanoparticles could be encapsulated in MFI zeolite via the in situ hydrothermal route and the presence of aluminum in zeolite framework did not influence the formation of palladium nanoparticles. For reference, palladium species were also introduced to S-1 and Na-ZSM-5 zeolites via wet impregnation. Through identical calcination and reduction processes, palladium particles, the dark dots in the images of Figure S5, with sizes from several to a dozen nanometers were observed on the surface of zeolite crystals.

3.2. Functionalities of Zeolite-Encapsulated Palladium Nanoparticles. For Pd@S-1, palladium centers appeared to be the sole active sites, and S-1 zeolite provided confinement effects on palladium centers and well-defined channels for catalytic reactions, while for Pd@Na-ZSM-5 and

DOI: 10.1021/acscatal.8b02276
ACS Catal. 2018, 8, 8578−8589

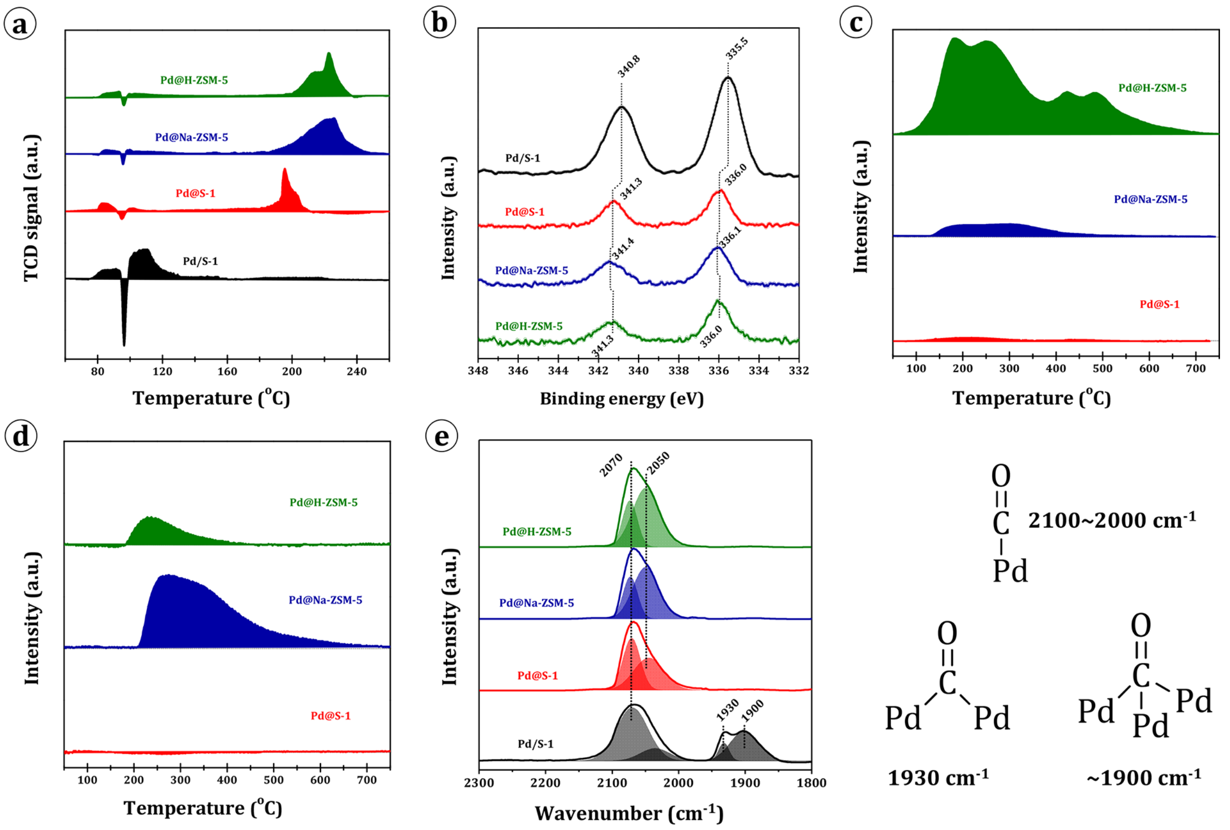

Figure 2. Physical−chemical properties of palladium-containing zeolites. (a) H_2-TPR profiles of samples after calcination; (b) Pd 3d XPS of samples; (c) NH_3-TPD and (d) CO_2-TPD profiles of samples; (e) FTIR spectra of CO adsorption on sample and corresponding CO adsorption configurations.

Pd@H-ZSM-5 additional base and acid sites might be provided by Na-ZSM-5 and H-ZSM-5 supports, respectively. We will focus on the functionalities of zeolite-encapsulated palladium nanoparticles in this section.

We first examined the reducibility of zeolite-encapsulated palladium species. After calcination in flowing air, palladium species should exist in the oxidized states, which can be reduced to metallic palladium by hydrogen. For Pd/S-1, the reduction of palladium species started from ~70 °C and ended at ~140 °C, involving a negative peak at ~95 °C due to the decomposition of PdH_x and the release of hydrogen (Figure 2a). The H/Pd ratio of 1.1 indicated that a considerable proportion of palladium species (almost half) were already reduced at 70 °C, in line with those observed for supported palladium catalyst,[22] while for zeolite-encapsulated palladium species, the major reduction peaks were observed in the temperature region of 170−250 °C. The retard in reduction of palladium species could be explained by their interaction with the zeolite framework. The H/Pd ratios of 1.6−1.9 (1.6 for Pd@S-1, 1.9 for Pd@Na-ZSM-5 and 1.7 for Pd@H-ZSM-5) indicated that only a small proportion of could be reduced by hydrogen at 50 °C, in great contrast to the case of Pd/S-1.

The chemical states of Pd nanoparticles encapsulated in zeolites were evaluated by XPS analysis. As shown in Figure 2b, the binding energy values of 335.5 and 340.8 eV were observed for reference Pd/S-1, corresponding to the $3d_{5/2}$ and $3d_{3/2}$ of metallic palladium, respectively.[30] For palladium nanoparticles encapsulated in zeolites, the palladium 3d binding energy values shifted significantly toward higher values by 0.5−0.6 eV due to the electron transfer from palladium to the zeolite framework, supporting the TPR results (Figure 2a). It was also noted that the intensities of the palladium 3d XPS signals in Pd@S-1, Pd@Na-ZSM-5, and Pd@H-ZSM-5 were much lower than that in Pd/S-1 with similar palladium loadings (Figure 2b). A rational explanation is that palladium species located on the outer surface of zeolite supports in Pd/zeolite, while they located inside zeolite crystals in Pd@zeolite, in accordance with literature reports.[19]

The exact location of palladium species on zeolite and the functionalities of zeolite channels were investigated through substrate-shape selective probe reactions. Pd/C and Pd/S-1 catalysts with palladium nanoparticles accessible to all molecules exhibited high activity in the hydrogenation of nitrobenzene (5.4 × 5.0 Å) and 1-nitronaphthalene (7.3 × 6.6 Å), as shown in Table S2. In contrast, palladium encapsulated in MFI zeolites (channel size: 5.6 × 5.3 Å), i.e., Pd@S-1 and Pd@Na-ZSM-5, only showed high activity for the nitrobenzene hydrogenation, with very low activity for 1-nitronaphthalene hydrogenation. Moreover, similar substrate-shape selectivity of Pd@S-1 and Pd@Na-ZSM-5 was explored in Suzuki coupling reactions, where a highly suppressed conversion of 2,4,6-trimethyl iodobenzene (7.2 × 7.1 Å) was observed compared with iodobenzene (5.2 × 5.0 Å) when coupling with 4-methoxyphenylboronic acid (Table S3). The distinct substrate-shape selectivity in both probe reactions unambiguously verified that most palladium nanoparticles had been successfully encapsulated inside zeolite crystals instead of anchoring to the outer surface of zeolites.

The additional functionalities provided by zeolite microenvironment, i.e., acid−base sites, were investigated by means

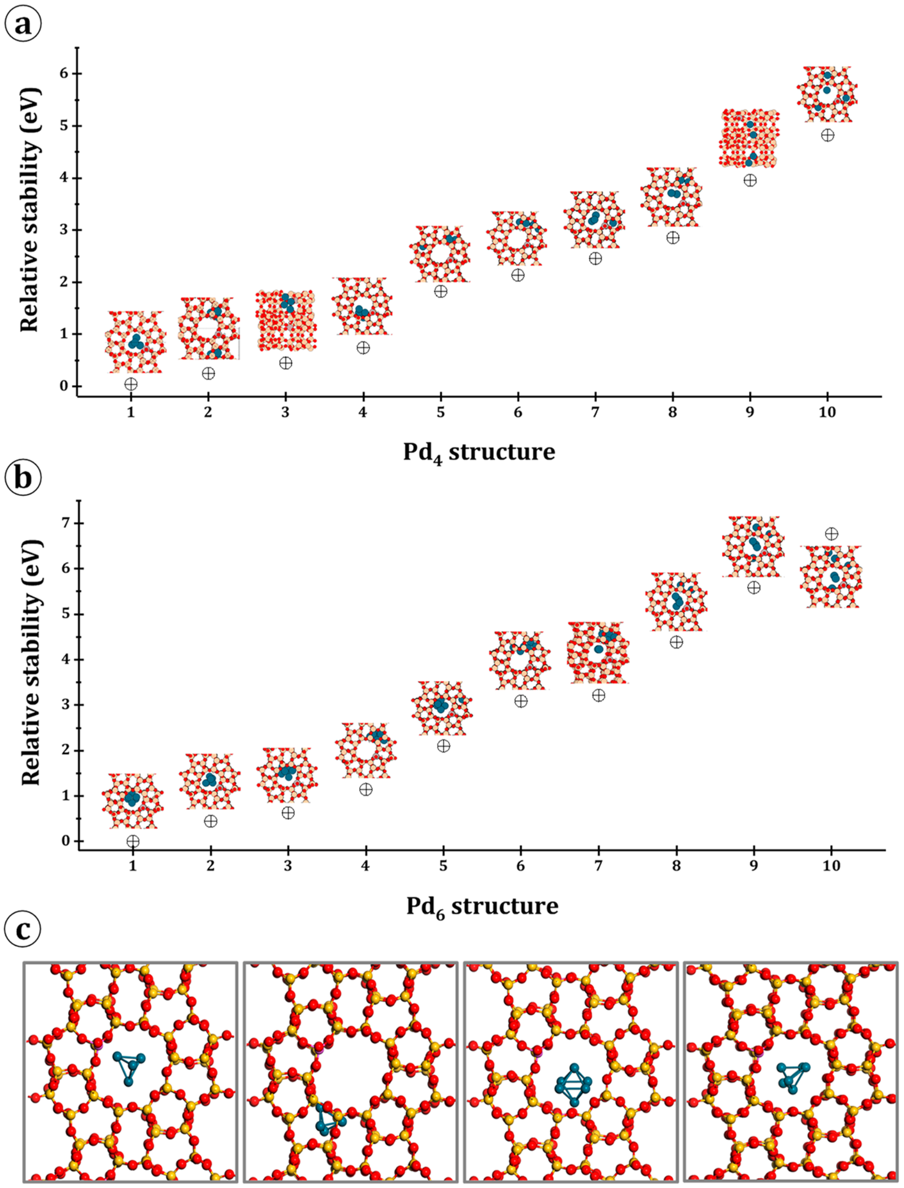

Figure 3. Simulated structure of zeolite encapsulated palladium clusters. (a) Ten representative structures of Pd_4@MFI from genetic algorithm calculations. (b) Ten representative structures of Pd_6@MFI from genetic algorithm calculations. (c) Feasible structure models of Pd@Na-ZSM-5.

of temperature-programed desorption of probe molecules. Pd@S-1 sample did not exhibit significant acidity or basicity, as revealed by the absence of desorption peaks of ammonia and carbon dioxide, respectively (Figure 2c,d). Weak ammonia desorption peaks in the temperature range of 150−450 °C (0.05 $mmol_{NH3}$/g) were observed in the NH_3-TPD profile of Pd@Na-ZSM-5. In contrast, strong ammonia desorption peaks in the temperature range of 100−450 °C (0.83 $mmol_{NH3}$/g) were observed for Pd@H-ZSM-5 (Figure 2c), confirming the existence of abundant acid sites in the sample. Compared with parent H-ZSM-5 (Figure S6), both the low-temperature and high-temperature ammonia desorption peaks split into two distinguishable peaks, which should be explained from the impacts of adjacent palladium nanoparticles on the strength of acid sites.[31] These observations, on the other hand, indicated the possible cooperation between acid sites and palladium nanoparticles in Pd@H-ZSM-5 during catalytic reaction. In the CO_2-TPD profiles (Figure 2d), significant carbon dioxide desorption peaks in the temperature region of 200−700 °C were observed for Pd@Na-ZSM-5, and the presence of abundant base sites (0.37 $mmol_{CO2}$/g) from zeolite framework (bridging oxogroup $[Si-O-Al]^-$ balanced by Na^+) could be proposed.

The local environment of palladium species was further studied by FTIR spectroscopy with CO adsorption (Figure 2e), which was reliable for the discrimination of highly dispersed metal centers and large metal aggregates.[16,32] For Pd/S-1, IR bands at 2100−2000, ∼1930, and ∼1900 cm^{-1} ascribed to atop-bonded, doubly bridge-bonded, and 3-fold bridge-bonded CO, respectively,[23,33] on the palladium surface were observed. These observations indicated the formation of palladium nanoparticles on the zeolite outer surface, as disclosed in TEM images (Figure S5). For palladium nanoparticles encapsulated in zeolites, only atop-bonded CO species (IR bands at 2100−2000 cm^{-1}) were observed, while doubly bridge-bonded (IR bands at ∼1930 cm^{-1}) and 3-fold bridge-bonded CO species (IR bands at ∼1900 cm^{-1}) were missing. Moreover, although exclusive atop-bonded CO species were formed on Pd@MFI, their specific constitution was different. More atop-bonded CO species on edge sites (IR bands at 2050 cm^{-1}) were formed on Pd@Na-ZSM-5 and Pd@H-ZSM-5, while more atop-bonded CO species (IR band at 2070 cm^{-1}) were formed on Pd@S-1.[34] That is, the presence of framework Al species could influence the adsorption configuration of CO on palladium to some extent. Overall, the palladium species should exist in the form of sub-nanometric particles in Pd@MFI, and the formation of large nanoparticles could be ruled out.[35] These seemed to coincide well with our experimental design, although they were somewhat inconsistent with the electron microscopic observations shown in Figure 1. We then came back to the results of electron microscopic analysis. In the high-resolution HAADF-STEM image of Pd@S-1 along the straight channels of MFI zeolite (Figure S7), both sub-nanometric palladium species ($d = \sim 0.8$ nm, marked with yellow circles) and palladium nanoparticles of ∼1.8 nm (marked with red circles) could be identified. Meanwhile, channel-size voids were found in palladium nanoparticles, pointing to sub-nanometric palladium species in the minimum dimension ($d = \sim 0.7$ nm). That is, palladium atoms (diameter of 3.6 Å) were successfully encapsulated in MFI zeolite channels (5.6 × 5.3 Å) during in situ synthesis, and they could migrate within zeolite channels during calcination and reduction step to form sub-nanometric palladium species, in good agreement with recent report on similar systems.[13]

The confinement of the MFI framework could limit the sizes of metal nanoparticles; thus, small cluster models or even single atoms were frequently applied in studying the active metals on ZSM-5.[36−38] Herein, two models, i.e., four and six Pd atoms per unit cell, respectively, were employed for global optimization calculations. In both cases, the Pd atoms tended to aggregate into Pd_4 and Pd_6 clusters, respectively, instead of monodispersed atoms or smaller clusters. In the case of Pd_4, the most stable structure was a tetrahedron-like cluster inside the straight 10-ring channel and the second most stable one was also a tetrahedron just beside the channel (Figure 3a). In the case of Pd_6, the most stable configuration was an octahedron-like cluster in 10-ring channel and a boatlike structure ranked second (Figure 3b). The genetic algorithm calculations offered many possible structures of different populations in each case (Table S4) and promised a potential cluster-rich configuration for Pd@MFI zeolites. According to the results from spectroscopic characterization and global optimization, the most feasible structure models of Pd@MFI are summarized in Figure 3c. In the as-obtained Pd@MFI sample, e.g., Pd@Na-ZSM-5, a mixture of Pd_4 and Pd_6 clusters with stable configuration should exist, which were observed as sub-nanometric palladium species encapsulated in zeolite.

3.3. Hydroconversion of Furfural over Zeolite-Encapsulated Palladium Nanoparticles. The unique catalytic properties of zeolite-encapsulated palladium nanoparticles were evaluated in the hydroconversion of FFL as a probe reaction. It is well-known that palladium catalysts can catalyze the hydroconversion of FFL while distinct reaction products might be obtained, as indicated by the reaction network in Scheme 1. Pd/S-1 (Figure 4a), Pd/Na-ZSM-5 (Figure 4b), and Pd/H-ZSM-5 (Figure 4c) exhibited similar catalytic performance in the hydroconversion of FFL, predominantly generating total hydrogenation products tetrahydrofuran, tetrahydrofuryl alcohol, and 2-methyltetrahydrofuran. These observations were in line with literature reports on palladium catalysts, e.g., Pd/C[39] and Pd/Al_2O_3,[22] with palladium nanoparticles on the surface of supports. We noted that even though acid−base sites were present in H-ZSM-5 and Na-ZSM-5 supports, they showed very limited impacts on the product distribution. Tentatively, the acid−base sites and palladium centers were not in close proximity to form cooperative effects during the reaction. In contrast to Pd/S-1, Pd@S-1 with quite similar chemical composition showed good selectivity toward FFL decarbonylation to furan (>70% at 175 °C), and the formation of total hydrogenation products was greatly suppressed, in good agreement with recent reports for this type of material.[14] This should be originated from the size- and site-dependent catalytic behaviors of metal centers encapsulated in zeolite,[40,41] which would be further interpreted in the next section. With the existence of acid−base sites in zeolite supports, zeolite-encapsulated palladium nanoparticles exhibited quite distinct selectivities in the hydroconversion of FFL. For Pd@Na-ZSM-5, FFL could be hydrogenated to FAL with high selectivity to >90% (at 175 °C), which was amazing for monometallic palladium catalysts.[22,23,39,42,43] Experimentally, the zeolite microenvironment could significantly modulate the reaction pathways and product distribution, while for Pd@H-ZSM-5, the protons from bridging hydroxyls in H-ZSM-5 (Si−OH-Al) could attack the oxygen atoms in furan rings and cause the ring opening via hydrogenolysis. As a result, 1,5-pentanediol (PDO) from hydrogenolysis-hydrogenation (∼30% at 175 °C), FAL from hydrogenation (∼30% at 175 °C), and furan from decarbonylation (∼30% at 175 °C) were produced. With prolonged reaction time, FAL and furan could not be further converted to straight-chain alcohols via hydrogenolysis (Figure S8). Moreover, total hydrogenation products, e.g., tetrahydrofurfuryl alcohol, were difficult to convert to straight chain alcohols under our reaction conditions (Figure S9).

Scheme 1. Reaction Network for the Hydroconversion of Furfural

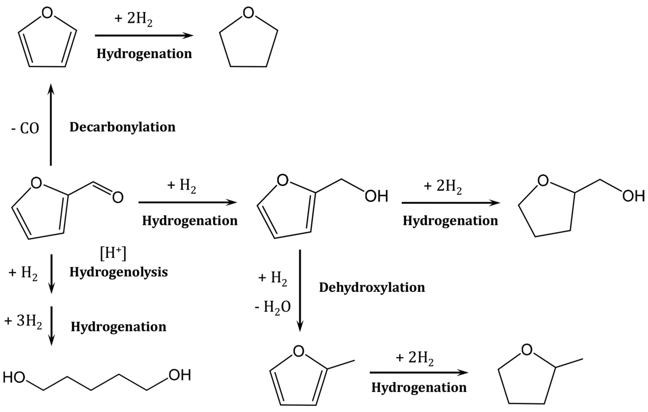

The different catalytic properties of various palladium catalysts in FFL hydroconversion are summarized in Table 1. Commercial Pd/C preferred to catalyze the total hydrogenation of FFL, accompanied by the significant condensation of furfural derives and the resulting low carbon balance. Zeolite supports, e.g., Na-ZSM-5 and H-ZSM-5, showed negligible activity in FFL hydroconversion, and palladium nanoparticles on the surface of zeolites (Pd/MFI) could catalyze the total hydrogenation of FFL. Zeolite-encapsulated palladium nanoparticles (Pd@MFI) exhibited comparable activity with palladium nanoparticles on zeolites (Pd/MFI), but the product

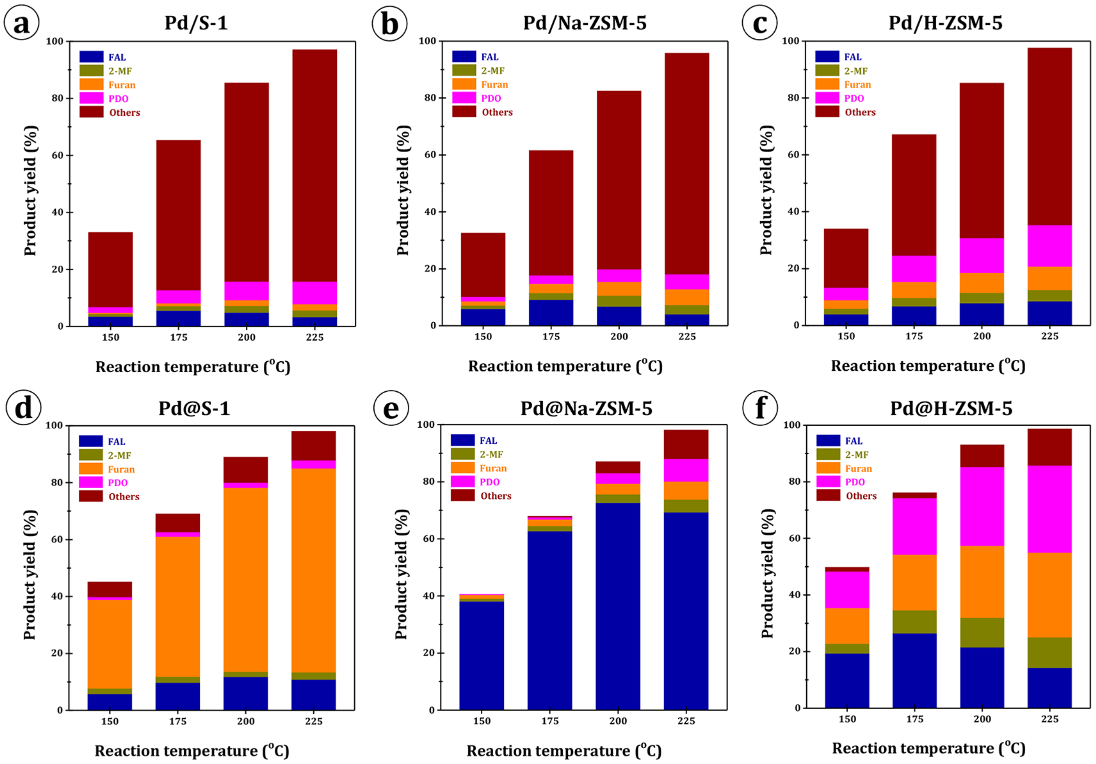

Figure 4. Catalytic performance of furfural hydroconversion over Pd/S-1 (a), Pd/Na-ZSM-5 (b), Pd/H-ZSM-5 (c), Pd@S-1 (d), Pd@Na-ZSM-5 (e), and Pd@H-ZSM-5 (f). Reaction conditions: 0.04 g of catalyst, 0.8 mmol of furfural, 3 mL of 2-propanol as solvent, 1 MPa H_2, reaction time = 3 h.

Table 1. Hydroconversion of FFL over Various Catalysts[a]

catalyst	reaction rate[b] (mmol/g/h)	selectivity[b] (%)					carbon balance[d]
		FAL	2-MF	furan	PDO	others[c]	
Pd/S-1	10.2	3.2	1.9	2.1	7.6	85.2	88
Pd@S-1	10.1	13.3	3.1	71.9	2.0	9.7	96
Pd/Na-ZSM-5	9.9	9.7	2.5	5.6	4.4	77.8	85
Pd@Na-ZSM-5	9.2	90.2	2.1	3.8	1.5	2.4	98
Pd/H-ZSM-5	10.3	9.9	4.5	8.4	13.8	63.4	82
Pd@H-ZSM-5	10.7	33.5	11.2	26.2	26.0	3.1	95
Na-ZSM-5	0.1	0	0	87.0	0	13.0	
H-ZSM-5	0.3	0	0	71.0	0	29.0	
Pd@S-1 and Na-ZSM-5[e]	5.5	12.4	3.0	73.2	1.1	10.3	96
Pd@S-1 and H-ZSM-5[e]	5.6	11.4	2.8	72.8	1.8	11.2	94
Pd@S-1 and NaOH[f]	10.2	12.8	3.1	72.4	1.9	9.8	96
Pd@S-1 and HCl[f]	10.5	12.5	3.2	72.1	2.3	9.9	95
Pd/C[g]	9.3	14.3	0	0	0	85.6	70

[a] Reaction conditions: 0.04 g of catalyst, 0.8 mmol of furfural, 3 mL of 2-propanol as solvent, 1 MPa H_2, T = 175 °C. [b] Data reported at FFL conversion of 10−20%. [c] Products from furan ring hydrogenation, with a few unknown products. [d] At FFL conversion of 50%. [e] 0.04 g of Pd@S-1 and 0.04 g Na-ZSM-5 or H-ZSM-5. [f] 0.04 g of Pd@S-1 and 25 μmol of NaOH or HCl. [g] Commercial product from Alfa Aesar with palladium loading of 5%.

distributions differed a lot. Pd@S-1 predominantly catalyzed the decarbonylation of FFL, generating furan as major product. Pd@Na-ZSM-5 predominantly catalyzed the hydrogenation of FFL to FAL. Pd@H-ZSM-5 could simultaneously catalyze the decarbonylation, the hydrogenation and hydrogenolysis of FFL, leading to complex products including furan, FAL, and PDO. Here, both the properties of palladium centers and zeolite microenvironment, e.g., the acid−base sites, played a crucial role in controlling the reaction pathways in FFL hydroconversion. Mixing Pd@S-1 with Na-ZSM-5 or H-ZSM-5 did not change the product distribution, probably due to the lack of cooperation between palladium centers and acid or base sites according to the so-called intimacy criterion.[44] The experiments of furfural hydroconversion catalyzed by the mixture of Pd@S-1 and NaOH or HCl were also performed. As shown in Table 1, the product selectivity of furfural hydroconversion on Pd@S-1 was not significantly changed even with the addition of liquid base or acid, and the reason for selectivity modulation would be discussed in the next section. On the whole, rational product selectivity control in FFL hydroconversion could be achieved by using palladium nanoparticles encapsulated in zeolites as model catalysts.

Table 2. Impacts of Hydrogen Pressure on the Hydroconversion of FFL[a]

catalyst	H_2 pressure (MPa)	reaction rate[b] (mmol/g/h)	selectivity[b] (%) FAL	2-MF	Furan	PDO	others[c]
Pd/S-1	0	3.1	0.6	2.1	91.5	0	5.8
Pd@S-1	1.0	10.1	13.3	3.1	71.9	2.0	9.7
	0.7	9.9	11.0	3.3	74.5	1.8	9.4
	0.4	9.8	7.5	3.0	78.6	1.9	9.0
	0.1	9.7	5.2	3.6	80.9	1.5	8.8
	0	7.4	0.7	2.3	91.7	0.1	5.2
Pd@Na-ZSM-5	1.0	9.2	90.2	2.1	3.8	1.5	2.4
	0.7	9.1	86.9	2.7	6.9	1.3	2.2
	0.4	9.1	81.5	2.9	12.5	1.2	1.9
	0.1	9.0	71.1	2.4	24.0	1.0	1.5
	0	7.3	1.9	3.0	90.6	0.1	4.4
Pd@H-ZSM-5	1.0	10.7	33.5	11.2	26.2	26.0	3.1
	0.7	10.6	31.5	11.6	28.4	25.5	3.0
	0.4	10.5	26.9	12.0	33.3	25.1	2.7
	0.1	10.4	21.3	12.5	39.6	24.3	2.3
	0	7.9	2.5	3.6	88.1	0.9	4.9

[a] Reaction conditions: 0.04 g of catalyst, 0.8 mmol of furfural, 3 mL of 2-propanol as solvent, 1 MPa He + H_2, T = 175 °C. [b] Data reported at FFL conversion of 10−20%. [c] Products from furan ring hydrogenation, with trace condensation products.

Although many products from FFL hydroconversion, e.g., furan, FAL, and PDO, have great industrial value, the precise selectivity control can significantly improve the economy in biomass upgrading.

We also investigated the impacts of hydrogen pressure on the hydroconversion of FFL over Pd@MFI. As shown in Table 2, the reaction rates of FFL hydroconversion over Pd@MFI decreased slightly with decreasing hydrogen pressure while the selectivity toward furan increased noticeably. All Pd@MFI catalysts showed considerable activity and good selectivities in FFL direct decarbonylation to furan in the absence of hydrogen, providing an alternative route for FFL upgrading. According to these experimental observations, FFL conversion to furan should proceed via direct decarbonylation, and the presence of hydrogen was beneficial to the reaction probably due to its promoting effects on CO removal from the surface.

Palladium nanoparticles encapsulated in MFI zeolites appeared to be promising catalysts for FFL upgrading, and in particular, Pd@Na-ZSM-5 was a robust catalyst for the selective hydrogenation of FFL to FAL. As expected, Pd@Na-ZSM-5 exhibited perfect recyclability in FFL hydroconversion, and no significant changes in FFL conversion and FAL selectivity could be observed in five reaction cycles (Figure 5a). Common problems leading to the deactivation of noble metal catalysts in liquid-phase reactions, i.e., particle sintering, metal leaching, and surface poisoning,[45] were not encountered for our Pd@Na-ZSM-5 catalyst. As shown in Figure 5b,c, the size and distribution of palladium nanoparticles encapsulated in Na-ZSM-5 remained almost unchanged after five complete recycles. Meanwhile, carbon balance of >95% was achieved for all reaction cycles, which was not reported in similar reaction systems. Moreover, Pd@S-1 and Pd@H-ZSM-5 exhibit perfect recyclability in FFL hydroconversion, as shown in Figure S10.

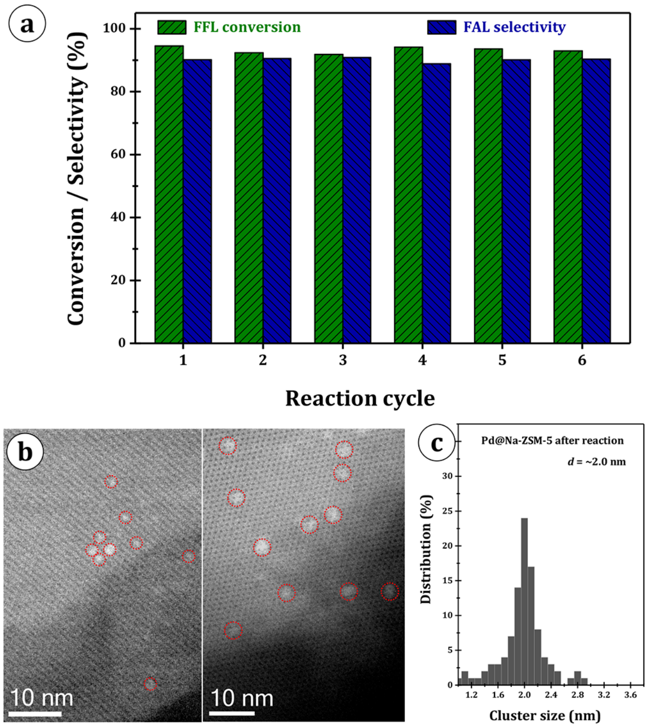

Figure 5. Recycling ability of Pd@Na-ZSM-5 in furfural hydroconversion. (a) Recycling test of furfural hydrogenation over Pd@Na-ZSM-5 catalyst. Reaction conditions: 0.04 g of catalyst, 0.8 mmol of furfural, 3 mL of 2-propanol as solvent, 1 MPa H_2, reaction time = 6 h; (b) HAADF-STEM image of Pd@Na-ZSM-5 after five recycles from different orientations; (c) corresponding size-distribution histogram of palladium nanoparticles from the HADDF-STEM image along the straight channels.

3.4. Catalysis of Zeolite-Encapsulated Sub-nanometric Palladium Species.

The adsorption of reactant molecules was examined to gain insight into the unique catalytic behaviors of zeolite-encapsulated sub-nanometric palladium species. We first investigated the adsorption behaviors of H_2 on palladium-containing zeolites. As shown in Figure 6a, specific H_2 desorption signals could be observed for all palladium-containing zeolites. H_2 adsorbed slightly more strongly on Pd@S-1 than that on Pd/S-1, which might be explained from the size-dependent effects of palladium. More importantly, the H_2 adsorption was significantly promoted by the presence of framework aluminum. A much higher amount

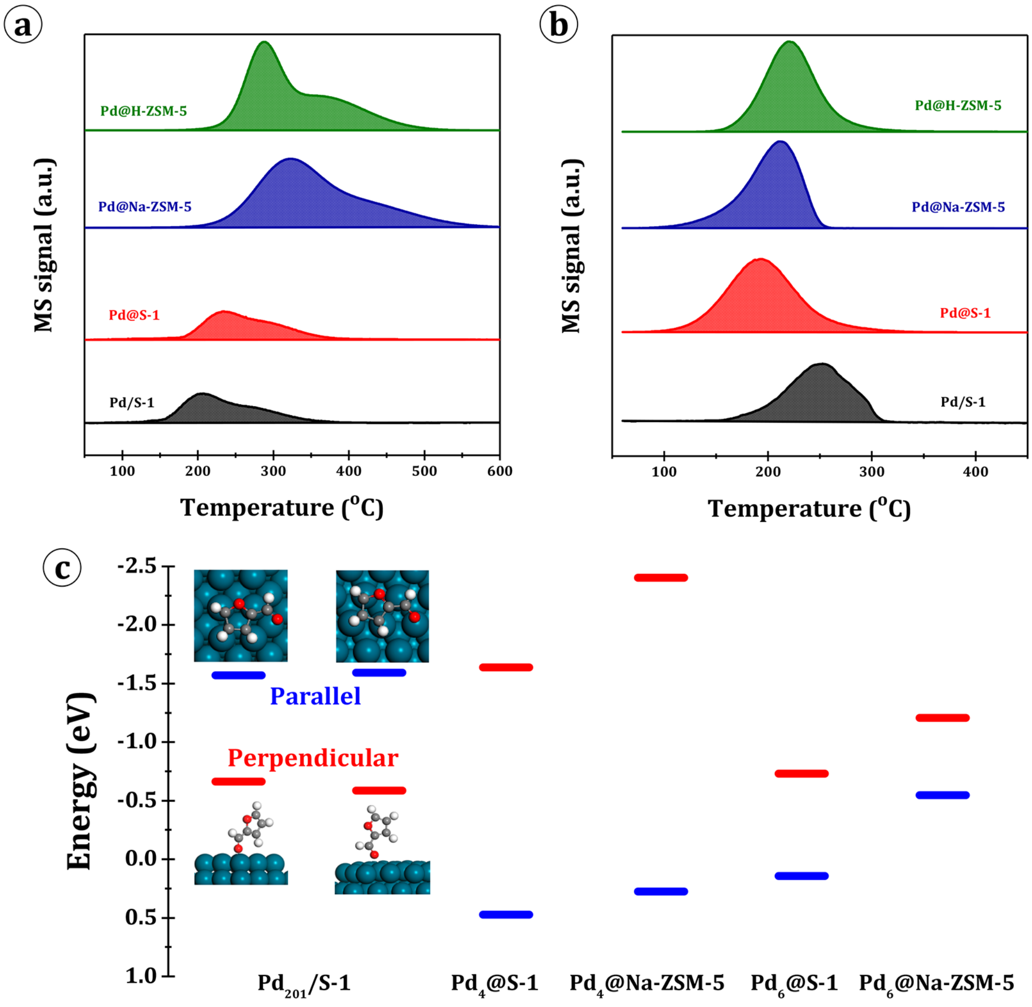

Figure 6. Physical−chemical properties of palladium-containing zeolites: (a) H_2-TPD profiles of Pd/S-1 and Pd@MFI; (b) furfural-TPD profiles of Pd/S-1 and Pd@MFI; (c) adsorption configurations of furfural on Pd_{201} clusters in Pd/S-1 and Pd_4 or Pd_6 clusters encapsulated in MFI zeolites.

of H_2 adsorbed more strongly on Pd@Na-ZSM-5 and Pd@H-ZSM-5 than that on Pd@S-1 (Figure 6a). Obviously, the zeolite framework participated in H_2 adsorption and activation, which was generally good for the hydrogenation reaction. In this context, we should treat Pd@MFI as a whole rather than sub-nanometric palladium species plus MFI zeolite support. The FFL-TPD profiles of Pd/S-1 and Pd@MFI were shown in Figure 6b. Typically, FFL adsorbed more strongly on Pd/S-1 than that on Pd@S-1 (60 °C difference in the desorption temperature). The presence of framework aluminum species could promote FFL adsorption on Pd@MFI to some extent, however, the FFL adsorption on Pd@Na-ZSM-5 and Pd@H-ZSM-5 was still weaker than that on Pd/S-1. Since FFL can adsorb on the palladium surface via oxygen of aldehyde group or via furan ring, DFT calculations were performed to reveal the exact adsorption configurations on different palladium-containing zeolites. As shown in Figure 6c, the FFL molecule preferred to adsorb on the Pd_{201} in Pd/S-1 via the furan ring with parallel configuration ($-1.57 \sim -1.59$ eV) over that via oxygen ($-0.66 \sim -0.59$ eV). The parallel configuration has been generally acknowledged in the adsorption of FFL on supported palladium nanoparticles.[22,23,46,47] In great contrast, for Pd_4@MFI and Pd_6@MFI, the perpendicular configuration was in preference to parallel configuration (Figure 6c), which should be explained by the cramped internal structure deep inside the zeolite framework and the hindrance of free movements. In addition, framework aluminum species could slightly promote FFL adsorption (see comparison between Pd@S-1 and Pd@Na-ZSM-5), consistent with FFL-TPD profiles (Figure 6b). The parallel configuration of FFL adsorption would unavoidably lead to the hydrogenation of furan ring, i.e., the over-hydrogenation of FFL while the perpendicular configuration was good for the hydrogenation of aldehyde group, which presented an intuitive explanation of the distinct selectivity in FFL hydroconversion over Pd/MFI and Pd@MFI (Figure 4).

On the other hand, despite of the perpendicular configuration of FFL adsorption on Pd@S-1 and Pd@Na-ZSM-5, the product distribution from FFL hydroconversion over these two catalysts was quite different (Figure 4), which should be explained from the degree of H_2 activation on these catalysts. As indicated by the H_2-TPD profile in Figure 6a, H_2 was inadequately activated on Pd@S-1, and accordingly, the strongly adsorbed FFL should undergo the direct decarbonylation to furan over Pd@S-1 (Figure 4, Table 1). The presence of H_2 could only increase the decarbonylation rate to some extent (Table 2) due to its promotion effect on CO removal. In contrast, with the presence of framework aluminum, H_2 was adequately activated on Pd@Na-ZSM-5 and involved in the hydrogenation of adsorbed FFL to FAL, as

DOI: 10.1021/acscatal.8b02276
ACS Catal. 2018, 8, 8578−8589

verified by catalytic data (Figure 4), while for Pd@H-ZSM-5 the protons from bridging hydroxyls in H-ZSM-5, i.e., Si-OH-Al, could attack the oxygen atoms in the furan rings and lead to secondary product PDO via ring-opening hydrogenolysis, as proposed in previous reports.[48−50]

On the whole, the zeolite microenvironment can show significant impacts on the adsorption of FFL and the activation of H_2 over encapsulated sub-nanometric palladium species, the latter being primarily responsible for the distinct reaction pathways in FFL hydroconversion over Pd@MFI (Scheme 1).

4. CONCLUSIONS

In summary, we have developed an efficient in situ strategy to zeolite-encapsulated palladium nanoparticles, i.e., Pd@MFI. Sub-nanometric palladium species are encapsulated inside the channels of MFI zeolites. Zeolites hosts can provide a specific microenvironment for encapsulated palladium species and, accordingly, alter their catalytic properties. Zeolite-encapsulated sub-nanometric palladium species exhibit high activity and excellent stability in the hydroconversion of furfural as a model reaction of biomass upgrading. More importantly, the product selectivity control in the context of furan, furfural alcohol, and 1,5-pentanediol is realized in furfural hydroconversion by changing the zeolite hosts of encapsulated palladium nanoparticles, i.e., silicalite-1, Na-ZSM-5, and H-ZSM-5. Temperature-programmed desorption studies and density functional theory calculations further reveal that both the adsorption of furfural and the activation of H_2 on encapsulated palladium species are significantly affected by the zeolite microenvironment, which accordingly leads to different pathways in furfural hydroconversion catalyzed by Pd@MFI.

As mentioned in the introduction, metal nanoparticles encapsulated in zeolites have exhibited significant advantages in activity, shape-selectivity, and stability over conventional supported catalysts. In this work, we further demonstrate the modulation of catalytic selectivity of encapsulated nanoparticles by tuning the zeolite microenvironment. All of these findings make zeolite-encapsulated metal nanoparticles promising catalysts for target reactions.

■ ASSOCIATED CONTENT

Ⓢ Supporting Information

The Supporting Information is available free of charge on the ACS Publications website at DOI: 10.1021/acscatal.8b02276.

> More characterization results of Pd@MFI zeolites and more catalytic data in furfural hydroconversion (PDF)

■ AUTHOR INFORMATION

Corresponding Author

*E-mail: lild@nankai.edu.cn.

ORCID

Jinlong Gong: 0000-0001-7263-318X
Weili Dai: 0000-0001-5752-0662
Landong Li: 0000-0003-0998-4061

Author Contributions

L.L. conceived the research ideas and directed the overall project. Y.C., W.D. and G.W. performed the experiments and analyzed the results. L.S., Z.-J.Z., and J.G. performed DFT calculations. All authors contributed to this manuscript.

Notes

The authors declare no competing financial interest.

■ ACKNOWLEDGMENTS

We thank Prof. Zhiyang Yu at Fuzhou University for help with microscopy analyses. This work was supported by the National Natural Science Foundation of China (21722303, 21421001), 111 Project (B12015, B18030), and the Fundamental Research Funds for the Central Universities (63185015).

■ REFERENCES

(1) Bond, G. C. Supported Metal Catalysts: Some Unsolved Problems. *Chem. Soc. Rev.* **1991**, *20*, 441−475.

(2) Gates, B. C. Supported Metal Clusters: Synthesis, Structure, and Catalysis. *Chem. Rev.* **1995**, *95*, 511−522.

(3) Munnik, P.; de Jongh, P. E.; de Jong, K. P. Recent Developments in the Synthesis of Supported Catalysts. *Chem. Rev.* **2015**, *115*, 6687−6718.

(4) Wanke, S. E.; Flynn, P. C. The Sintering of Supported Metal Catalysts. *Catal. Rev.: Sci. Eng.* **1975**, *12*, 93−135.

(5) Newton, M. A.; Belver-Coldeira, C.; Martínez-Arias, A.; Fernández-García, M. Dynamic in situ Observation of Rapid Size and Shape Change of Supported Pd Nanoparticles during CO/NO Cycling. *Nat. Mater.* **2007**, *6*, 528−532.

(6) Prieto, G.; Zečević, J.; Friedrich, H.; de Jong, K. P.; de Jongh, P. E. Towards Stable Catalysts by Controlling Collective Properties of Supported Metal Nanoparticles. *Nat. Mater.* **2013**, *12*, 34−39.

(7) Sachtler, W. M. H.; Zhang, Z. Zeolite-supported Transition Metal Catalysts. *Adv. Catal.* **1993**, *39*, 129−220.

(8) Zhan, B. Z.; Iglesia, E. RuO_2 clusters within LTA Zeolite Cages: Consequences of Encapsulation on Catalytic Reactivity and Selectivity. *Angew. Chem., Int. Ed.* **2007**, *46*, 3697−3700.

(9) Choi, M.; Wu, Z.; Iglesia, E. Mercaptosilane-assisted Synthesis of Metal Clusters within Zeolites and Catalytic Consequences of Encapsulation. *J. Am. Chem. Soc.* **2010**, *132*, 9129−9137.

(10) Goel, S.; Wu, Z.; Zones, S. I.; Iglesia, E. Synthesis and Catalytic Properties of Metal Clusters Encapsulated within Small-pore (SOD, GIS, ANA) Zeolites. *J. Am. Chem. Soc.* **2012**, *134*, 17688−17695.

(11) Wu, Z.; Goel, S.; Choi, M.; Iglesia, E. Hydrothermal Synthesis of LTA-encapsulated Metal Clusters and Consequences for Catalyst Stability, Reactivity, and Selectivity. *J. Catal.* **2014**, *311*, 458−468.

(12) Goel, S.; Zones, S. I.; Iglesia, E. Encapsulation of Metal Clusters within MFI via Interzeolite Transformations and Direct Hydrothermal Syntheses and Catalytic Consequences of their Confinement. *J. Am. Chem. Soc.* **2014**, *136*, 15280−15290.

(13) Wang, N.; Sun, Q.; Bai, R.; Li, X.; Guo, G.; Yu, J. In situ Confinement of Ultrasmall Pd Clusters within Nanosized Silicalite-1 Zeolite for Highly Efficient Catalysis of Hydrogen Generation. *J. Am. Chem. Soc.* **2016**, *138*, 7484−7487.

(14) Wang, C.; Wang, L.; Zhang, J.; Wang, H.; Lewis, J. P.; Xiao, F. S. Product Selectivity Controlled by Zeolite Crystals in Biomass Hydrogenation over a Palladium Catalyst. *J. Am. Chem. Soc.* **2016**, *138*, 7880−7883.

(15) Moliner, M.; Gabay, J. E.; Kliewer, C. E.; Carr, R. T.; Guzman, J.; Casty, G. L.; Serna, P.; Corma, A. Reversible Transformation of Pt Nanoparticles into Single Atoms inside High-silica Chabazite Zeolite. *J. Am. Chem. Soc.* **2016**, *138*, 15743−15750.

(16) Liu, L.; Diaz, U.; Arenal, R.; Agostini, G.; Concepcion, P.; Corma, A. Generation of Subnanometric Platinum with High Stability during Transformation of a 2D Zeolite into 3D. *Nat. Mater.* **2017**, *16*, 132−138.

(17) Laursen, A. B.; Hojholt, K. T.; Lundegaard, L. F.; Simonsen, S. B.; Helveg, S.; Schüth, F.; Paul, M.; Grunwaldt, J. D.; Kegnaes, S.; Christensen, C. H.; Egeblad, K. Substrate Size-selective Catalysis with Zeolite-encapsulated Gold Nanoparticles. *Angew. Chem., Int. Ed.* **2010**, *49*, 3504−3507.

(18) Cui, T. L.; Ke, W. Y.; Zhang, W. B.; Wang, H. H.; Li, X. H.; Chen, J. S. Encapsulating Palladium Nanoparticles inside Mesoporous

MFI Zeolite Nanocrystals for Shape-selective Catalysis. *Angew. Chem., Int. Ed.* **2016**, *55*, 9178−9182.

(19) Liu, C.; Liu, J.; Yang, S.; Cao, C.; Song, W. Palladium Nanoparticles Encapsulated in a Silicalite-1 Zeolite Shell for Size-selective Catalysis in Liquid-phase Solution. *ChemCatChem* **2016**, *8*, 1279−1282.

(20) Zhang, J.; Wang, L.; Shao, Y.; Wang, Y.; Gates, B. C.; Xiao, F. S. A Pd@zeolite Catalyst for Nitroarene Hydrogenation with High Product Selectivity by Sterically Controlled Adsorption in the Zeolite Micropores. *Angew. Chem., Int. Ed.* **2017**, *56*, 9747−9751.

(21) Besson, M.; Gallezot, P.; Pinel, C. Conversion of Biomass into Chemicals over Metal Catalysts. *Chem. Rev.* **2014**, *114*, 1827−1870.

(22) Bhogeswararao, S.; Srinivas, D. Catalytic Conversion of Furfural to Industrial Chemicals over Supported Pt and Pd Catalysts. *J. Catal.* **2015**, *327*, 65−77.

(23) Rogers, S. M.; Catlow, C. R. A.; Chan-Thaw, C. E.; Chutia, A.; Jian, N.; Palmer, R. E.; Perdjon, M.; Thetford, A.; Dimitratos, N.; Villa, A.; Wells, P. P. Tandem Site- and Size-controlled Pd Nanoparticles for the Directed Hydrogenation of Furfural. *ACS Catal.* **2017**, *7*, 2266−2274.

(24) Yu, Z.; Cantwell, P.; Gao, Q.; Yin, D.; Zhang, Y.; Zhou, N.; Rohrer, G.; Widom, M.; Luo, J.; Harmer, M. Segregation-induced ordered superstructures at general grain boundaries in a nickel-bismuth alloy. *Science* **2017**, *358*, 97−101.

(25) Kresse, G.; Furthmüller, J. Efficiency of Ab-initio Total Energy Calculations for Metals and Semiconductors Using a Plane-wave Basis Set. *Comput. Mater. Sci.* **1996**, *6*, 15−50.

(26) Blöchl, P. E. Projected Augmented-wave Method. *Phys. Rev. B: Condens. Matter Mater. Phys.* **1994**, *50*, 17953−17979.

(27) Kresse, G.; Joubert, D. From Ultrasoft Pseudopotentials to the Projector Augmented-wave Method. *Phys. Rev. B: Condens. Matter Mater. Phys.* **1999**, *59*, 1758−1775.

(28) Sierka, M. Synergy between Theory and Experiment in Structure Resolution of Low-dimensional Oxides. *Prog. Surf. Sci.* **2010**, *85*, 398−434.

(29) Johnston, R. L. Evolving Better Nanoparticles: Genetic Algorithms for Optimising Cluster Geometries. *Dalton Trans.* **2003**, *22*, 4193−4207.

(30) Crist, B. V. *Handbook of Monochromatic XPS Spectra*; Wiley: New York, 2011.

(31) Santi, D.; Rabl, S.; Calemma, V.; Dyballa, M.; Hunger, M.; Weitkamp, J. Effect of Noble Metals on the Strength of Brønsted Acid Sites in Bifunctional Zeolites. *ChemCatChem* **2013**, *5*, 1524−1530.

(32) Hadjiivanov, K.; Vayssilov, G. N. Characterization of Oxide Surfaces and Zeolites by Carbon Monoxide as an IR Probe Molecule. *Adv. Catal.* **2002**, *47*, 307−501.

(33) Wang, X.; Wu, G.; Guan, N.; Li, L. Supported Pd Catalysts for Solvent-free Benzyl Alcohol Selective Oxidation: Effects of Calcination Pretreatments and Reconstruction of Pd Sites. *Appl. Catal., B* **2012**, *115*−*116*, 7−15.

(34) Lear, T.; Marshall, R.; Lopez-Sanchez, J. A.; Jackson, S. D.; Klapötke, T. M.; Bäumer, M.; Rupprechter, G.; Freund, H.-J.; Lennon, D. The Application of Infrared Spectroscopy to Probe the Surface Morphology of Alumina-supported Palladium Catalysts. *J. Chem. Phys.* **2005**, *123*, 174706.

(35) Lang, R.; Li, T.; Matsumura, D.; Miao, S.; Ren, Y.; Cui, Y. T.; Tan, Y.; Qiao, B.; Li, L.; Wang, A.; Wang, X.; Zhang, T. Hydroformylation of Olefins by a Rhodium Single-atom Catalyst with Activity Comparable to $RhCl(PPh_3)_3$. *Angew. Chem., Int. Ed.* **2016**, *55*, 16054−16058.

(36) Heyden, A.; Peters, B.; Bell, A. T.; Keil, F. J. Comprehensive DFT Study of Nitrous Oxide Decomposition over Fe-ZSM-5. *J. Phys. Chem. B* **2005**, *109*, 1857−1873.

(37) Zhidomirov, G. M.; Shubin, A. A.; Milov, M. A.; Kazansky, V. B.; van Santen, R. A.; Hensen, E. J. M. Cluster Model DFT Study of CO Adsorption to Dallium Ions in Ga/HZSM-5. *J. Phys. Chem. C* **2008**, *112*, 3321−3326.

(38) Lou, Y.; Ma, J.; Hu, W.; Dai, Q.; Wang, L.; Zhan, W.; Guo, Y.; Cao, X.-M.; Guo, Y.; Hu, P.; Lu, G. Low-temperature Methane Combustion over Pd/H-ZSM-5: Active Pd Sites with Specific Electronic Properties Modulated by Acidic Sites of H-ZSM-5. *ACS Catal.* **2016**, *6*, 8127−8139.

(39) Fulajtárova, K.; Soták, T.; Hronec, M.; Vávra, I.; Dobročka, E.; Omastová, M. Aqueous Phase Hydrogenation of Furfural to Furfuryl Alcohol over Pd−Cu Catalysts. *Appl. Catal., A* **2015**, *502*, 78−85.

(40) Vorotnikov, V.; Mpourmpakis, G.; Vlachos, D. G. DFT Study of Furfural Conversion to Furan, Furfuryl Alcohol, and 2-Methylfuran on Pd(111). *ACS Catal.* **2012**, *2*, 2496−2504.

(41) Pushkarev, V. V.; Musselwhite, N.; An, K.; Alayoglu, S.; Somorjai, G. A. High Structure Sensitivity of Vapor-phase Furfural Decarbonylation/hydrogenation Reaction Network as a Function of Size and Shape of Pt Nanoparticles. *Nano Lett.* **2012**, *12*, 5196−5201.

(42) Nakagawa, Y.; Takada, K.; Tamura, M.; Tomishige, K. Total Hydrogenation of Furfural and 5-Hydroxymethylfurfural over Supported Pd−Ir Alloy Catalyst. *ACS Catal.* **2014**, *4*, 2718−2726.

(43) Thompson, S. T.; Lamb, H. H. Palladium−rhenium Catalysts for Selective Hydrogenation of Furfural: Evidence for an Optimum Surface Composition. *ACS Catal.* **2016**, *6*, 7438−7447.

(44) Pino, N.; Sitthisa, S.; Tan, Q.; Souza, T.; López, D.; Resasco, D. E. Structure, Activity, and Selectivity of Bimetallic Pd-Fe/SiO_2 and Pd-Fe/γ-Al_2O_3 Catalysts for the Conversion of Furfural. *J. Catal.* **2017**, *350*, 30−40.

(45) Pang, S. H.; Medlin, J. W. Adsorption and Reaction of Furfural and Furfuryl Alcohol on Pd(111): Unique Reaction Pathways for Multifunctional Reagents. *ACS Catal.* **2011**, *1*, 1272−1283.

(46) Weisz, P. B. Polyfunctional Heterogeneous Catalysis. *Adv. Catal.* **1962**, *13*, 137−190.

(47) Besson, M.; Gallezot, P. Deactivation of Metal Catalysts in Liquid Phase Organic Reactions. *Catal. Today* **2003**, *81*, 547−559.

(48) Zhao, C.; Lercher, J. A. Upgrading Pyrolysis Oil over Ni/HZSM-5 by Cascade Reactions. *Angew. Chem., Int. Ed.* **2012**, *51*, 5935−5940.

(49) Lange, J.-P.; van de Graaf, W. D.; Haan, R. J. Conversion of Ffurfuryl Alcohol into Ethyl Levulinate Using Solid Acid Catalysts. *ChemSusChem* **2009**, *2*, 437−441.

(50) Mellmer, M. A.; Gallo, J. M. R.; Alonso, D. M.; Dumesic, J. A. Selective Production of Levulinic Acid from Furfuryl Alcohol in THF Solvent Systems over H-ZSM-5. *ACS Catal.* **2015**, *5*, 3354−3359.